High strength and formable Mg–6.2Zn–0.5Zr–0.2Ca alloy sheet processed by twin roll casting

T. Bhattacharjee [a,b], B.-C Suh [c], T.T. Sasaki [b], T. Ohkubo [b], N.J. Kim [d], K. Hono [a,b,*]

[a] Graduate School of Pure and Applied Sciences, University of Tsukuba, Tsukuba 305-8577, Japan
[b] National Institute for Materials Science, 1-2-1 Sengen, Tsukuba 305-0047, Japan
[c] Center for Advanced Aerospace Materials, POSTECH, Pohang 790-784, Republic of Korea
[d] Graduate Institute of Ferrous Technology and CAAM, POSTECH, Pohang 790-784, Republic of Korea

ARTICLE INFO

ABSTRACT

Twin roll cast and hot rolled Mg–6.2 wt%Zn alloys microalloyed with Zr, Ca, and Ag show tensile yield strength exceeding 300 MPa in the T6 (peak-aged) condition with reasonable formability in the T4 condition. The addition of Zr and Ca plays a critical role in the development of weak textured recrystallized microstructure in Mg–6.2 wt%Zn alloys so Mg–6.2Zn–0.5Zr–0.2Ca (wt%) alloy shows equivalent mechanical properties with Mg–6.2Zn–0.5Zr–0.2Ca–0.4Ag (wt%) alloy even without expensive Ag.

1. Introduction

The use of light weight magnesium alloys as structural materials in the transportation sector is considered to be effective in improving fuel efficiency by weight reduction. The main barrier for the application of the wrought magnesium alloys is their limited room temperature formability. Recent investigation has shown that alloying with rare earth elements improves the formability by weakening the basal texture [1]. The next challenge is to develop low-cost high strength and formable wrought magnesium alloys by avoiding expensive rare earth metals. Among various rare earth free magnesium alloys, Mg–Zn based alloys are very promising for its good age hardening characteristics [2–6]. Mendis et al. reported high yield strength over 300 MPa in T6 aged Mg–6.1Zn–0.4Ag–0.2Ca–0.6Zr (wt%) alloy (ZKQX6000) in the form of extruded bar and twin roll cast and hot rolled sheet [7,8]. The twin roll cast and hot rolled (TRC-HR) ZKQX6000 alloy sheets exhibited an excellent formability in the T4 condition, a high yield strength (σ_{ys}) of 320 MPa and an ultimate tensile strength (σ_{uts}) of ~342 MPa with an elongation to failure (ε_f) of 17% after an artificial aging (T6), which was expected to open up a possibility for the development of heat treatable wrought magnesium based alloy [8]. The T4 and

T6 treated ZKQX alloys contain fine Mg(Zn,Zr) precipitates, which control the microstructure during wrought processing [7,9]. Our recent investigation has shown that the same precipitates can be observed in the T4 and T6 treated Mg–6.2Zn–0.6Zr or ZK60 alloy [10]. However, the formability appears to be improved by the addition of Ca to the binary Mg–Zn alloy [11]. Since the understanding of the role of individual alloying elements is important for alloy development, we investigated the microstructure and mechanical properties of twin roll cast and hot rolled (TRC-HR) Mg–6.2Zn (wt%) (Z6), Mg–6.2Zn–0.5Zr (wt%) (ZK60), Mg–6.2Zn–0.5Zr–0.2Ca (wt%) (ZKX600) and Mg–6.2Zn–0.5Zr–0.4Ag–0.2Ca (wt%) (ZKQX6000) alloys in order to understand the effect of individual microalloying elements.

2. Experimental

Alloy ingots with nominal compositions (in wt%) of Mg–6.2Zn (Z6), Mg–6.2Zn–0.5Zr (ZK60), Mg–6.2Zn–0.5Zr–0.2Ca (ZKX600) and Mg–6.2Zn–0.5Zr–0.4Ag–0.2Ca (ZKQX6000) were prepared by induction melting in an argon atmosphere using a steel crucible. Table 1 summarizes the chemical compositions of these alloys in wt% and at%. The ingots were then remelted under a mixture of CO_2 and SF_6 and transferred into a preheated tundish held at 680–700 °C followed by twin roll casting. The roll gap was set at 1.8 mm and roll speed was 4 m/min. The cast sheets were then

* Corresponding author at: National Institute for Materials Science, 1-2-1 Sengen, Tsukuba 305-0047, Japan.
E-mail address: kazuhiro.hono@nims.go.jp (K. Hono).

Table 1
The nomenclatures and the nominal compositions of the alloys used in this work.

nomenclature	Atomic%	Mass%
Z6	Mg–2.4Zn	Mg–6.2Zn
ZK60	Mg–2.4Zn–0.1Zr	Mg–6.2Zn–0.5Zr
ZKX600	Mg–2.4Zn–0.1Zr–0.1Ca	Mg–6.2Zn–0.5Zr–0.2Ca
ZKQX6000	Mg–2.4Zn–0.1Zr–0.1Ca–0.1Ag	Mg–6.2Zn–0.5Zr–0.2Ca–0.4Ag

homogenized at 330 °C for 2 h and then hot rolled at 300 °C for three passes with a total reduction of 50%. The rolled sheet samples were then heat-treated at 400 °C for 30 min and quenched into cold water (T4) and finally aged at 160 °C for 0.5–1000 h in a silicone oil bath. The Vickers hardness was measured for all the samples with 10 individual indentations with a 0.5 kg load. Tensile properties were measured using flat tensile specimens with a gauge length of 12.5 mm, gauge thickness of 1 mm and gauge width of 5 mm at a strain rate of 6.4×10^{-4} s^{-1} along the rolling direction (RD). Stretch formability was evaluated by the limiting dome height (LDH) value obtained by the Erichsen cupping test (square-shaped specimen of size 50 mm $\times$ 50 mm). The punch diameter and speed used were 20 mm and 0.1 mm s^{-1} respectively. Silicone oil was used as a lubricant. The crystallographic macrotexture of the alloys were analyzed on the mid-section of the specimens by X-ray diffraction (XRD) using Cu Kα radiation with a measuring grid of $5° \times 5°$ in both polar and azimuthal rotations of the specimen to a maximum tilt of 90°. The pole figure data analyses were done by using Labotex 3.0 software. Microstructure observations were performed using optical microscope (OM), electron back scattered diffraction (EBSD), transmission electron microscope (TEM) and three dimensional atom probe (3DAP). EBSD was carried out by using Carl Zeiss CrossBeam 1540EsB field-emission scanning electron microscope equipped with a HKL EBSD detector along the normal direction-rolling direction (ND–RD) plane of the samples. EBSD data analyses were performed using TSL OIM 7.0 software. TEM observations were conducted using FEI Tecnai T20 and Titan G^2 80-200 microscopes operating at 200 kV. TEM specimens were prepared using twin jet electro-polishing using a solution of 300 ml 2-butoxy ethanol, 15.9 g lithium chloride, 33.5 g of magnesium perchlorate in 1500 ml methanol at a temperature of ~ -45 °C as well as ion-polishing using Gatan Precision Ion Polishing System (PIPS). Three dimensional atom probe (3DAP) analyses were carried out with a locally built laser assisted wide angle atom probe using a femtosecond laser pulse at a wavelength of 343 nm [12]. Square bars with dimensions of $\sim 0.5 \times 0.5 \times 15$ mm^3 were cut from the bulk samples and electropolished to prepare sharp needle-like specimens for atom probe analyses. The 3DAP analyses were performed in an ultrahigh-vacuum condition ($< 1 \times 10^{-8}$ Pa) at a temperature of 25 K.

3. Results

Fig. 1 shows the variation in Vickers hardness values as a function of aging time. The as-rolled hardness of Z6 alloy is 75 ± 1 HV whereas ZK60, ZKX600 and ZKQX6000 alloys has the as-rolled hardness of 90 ± 2 HV. After a T4 treatment at 400 °C for 30 min, the hardness decreases to 53 ± 1 HV for Z6 alloy, 65 ± 1 HV for ZK60 alloy, 66 ± 1 HV for ZKX600 alloy and 71 ± 1 HV for ZKQX6000 alloy. Upon artificial aging at 160 °C, the hardness starts to increase after 30 min of aging and all the alloys reach their peak hardness values at an aging time of 24 h. The peak-aged values are around 75 ± 2 HV for Z6 alloy, 80 ± 2 HV
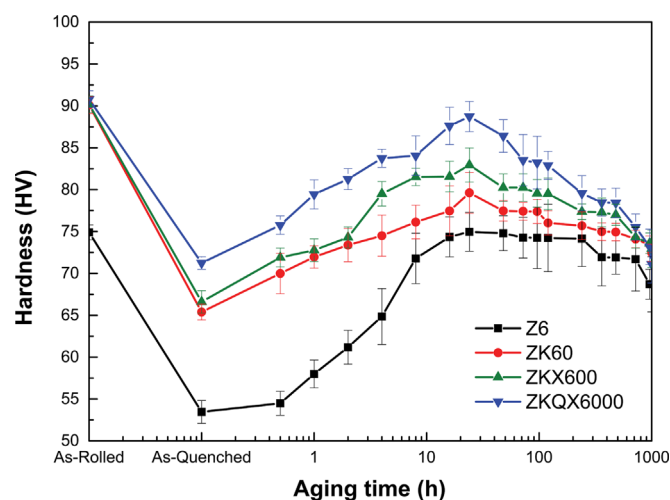

Fig. 1. The age hardening response of the Z6, ZK60, ZKX600 and ZKQX6000 alloy at 160 °C.

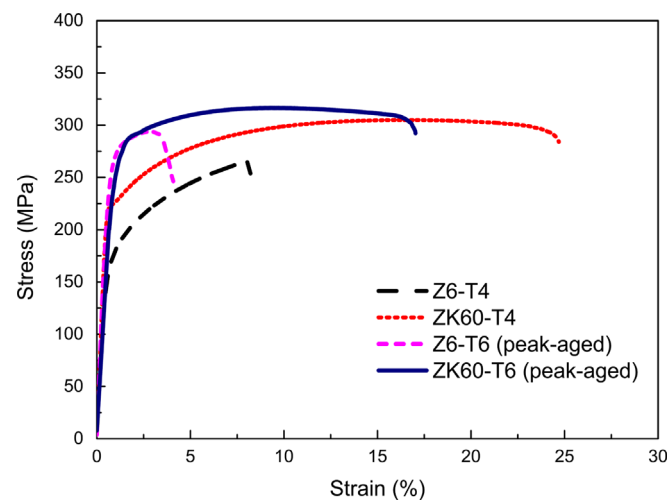**Fig. 2.** Tensile stress–strain curves of Z6 and ZK60 at T4 condition (400 °C for 30 min) and T6 (peak-aged) condition.

for ZK60 alloy, 83 ± 2 HV for ZKX600 alloy, and 89 ± 2 HV for ZKQX6000 alloy.

Fig. 2 shows the tensile stress–strain curves of Z6 and ZK60 alloys in T4 and peak-aged conditions. Table 2 summarizes the tensile properties of all the alloys in the present investigation. The T4 treated Z6 alloy shows a yield strength (0.2% offset strength), σ_{ys}, of 163 MPa with elongation to failure of 8.2%. Upon peak aging, σ_{ys} of the Z6 alloy increases to 246 MPa at an expense of elongation to failure, 4.2%. ZK60 alloy shows a σ_{ys} of 220 MPa in the T4 condition with elongation to failure of 24.0%. Upon peak aging, σ_{ys} increased to 270 MPa and has an elongation to failure of 17.0%.

Fig. 3 shows the tensile stress–strain curves of the ZKX600 and ZKQX6000 alloys in the T4 and peak-aged conditions. T4 treated ZKX600 and ZKQX6000 alloys show σ_{ys} of 210 MPa and 225 MPa with elongation to failure of 15.0% and 13.4%, respectively. Upon peak aging, σ_{ys} of ZKX600 alloy reaches 286 MPa, which is very close to that of the ZKQX6000 alloy, 300 MPa. The ZKX600 alloy also exhibits larger elongation to failure of 15.0% in comparison to ZKQX6000 alloy which shows 12.4% in the peak-aged condition.

Fig. 4 shows the LDH values measured by Erichsen cup test as a function of tensile yield strength (T4 condition). For comparison, the LDH values of other TRC and rolled Mg alloys are also shown [13]. Note that a larger punch diameter of 30 mm was used instead

Table 2
Tensile properties of the investigated alloys in T4 and T6 (peak-aged) condition.

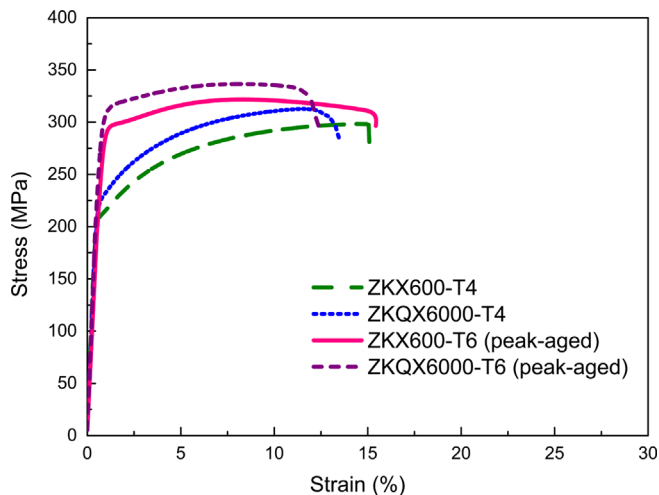| Alloy	T4 (400 °C–30 min)			T6 (peak-aged)		
	σ_{ys} (MPa)	σ_{uts} (MPa)	ε_f (%)	σ_{ys} (MPa)	σ_{uts} (MPa)	ε_f (%)
Z6	163	264	8.2	246	294	4.2
ZK60	220	305	24.0	270	316	17.0
ZKX600	210	300	15.0	286	321	15.0
ZKQX6000	225	312	13.4	300	336	12.4

Fig. 3. Tensile stress–strain curves of ZKX600 and ZKQX6000 at T4 condition (400 °C for 30 min) and T6 (peak-aged) condition.
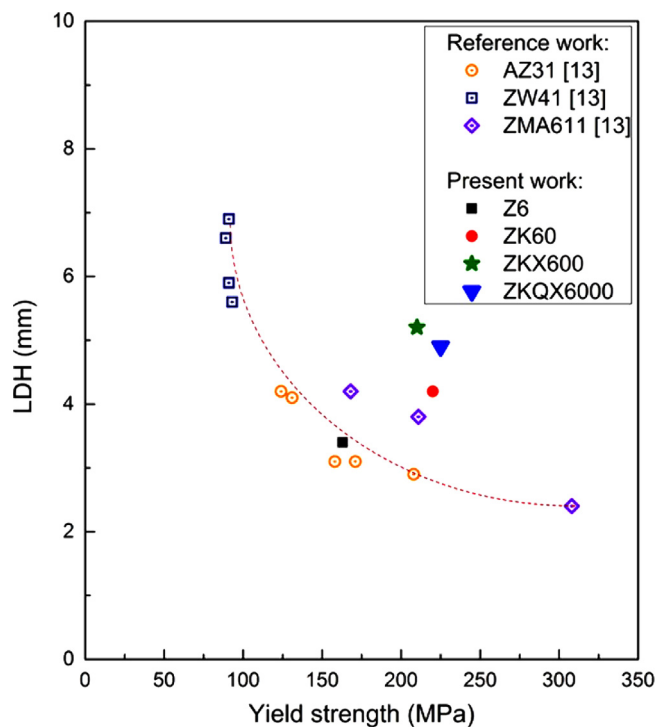

Fig. 4. Plot of Erichsen cup tested LDH values as a function of tensile yield strength (T4 condition).

of 20 mm used in the present study for the Erichsen cup test in the reference [13]. The LDH values of Z6, ZK60, ZKX600 and ZKQX6000 alloys are 3.4, 4.2, 5.2 and 4.9 mm, respectively. While the LDH generally decreases with an increase in yield strength (Fig. 4), T4 treated ZK60, ZKX600 and ZKQX6000 alloys exhibits larger LDH values in spite of their higher strength in comparison to other TRC-HR alloys such as Mg–3Al–1Zn (AZ31) and Mg–6Zn–1Al–1Mn (ZMA611) alloys. Particularly, the ZKX600 alloy exhibits the highest LDH value among the alloys in the present study even without the addition of Ag.

Fig. 5(a–d) shows the optical microstructures and (0001) X-ray pole figures of Z6, ZK60, ZKX600 and ZKQX6000 alloys in the T4 condition taken along the ND-RD plane. The Z6 alloy shows equiaxed recrystallized grains of $30.0 \pm 10.0\,\mu m$ with a strong basal texture in which the (0001) plane is parallel to the rolling plane (Fig. 5(a)). ZK60, ZKX600 and ZKQX6000 alloys show recrystallized grains of around $7.0 \pm 3.0\,\mu m$ in addition to the coarse unrecrystallized grains elongated along the rolling direction (Fig. 5(b–d)). The areal fraction of the unrecrystallized grains increases by the addition of Ag and Ca to the ZK60 alloy. The formation of twins within these grains as marked by black circles in Fig. 5(c) and (d). Interestingly, the (0001) poles split along the RD in the ZK60, ZKX600 and ZKQX6000 alloys as shown in Fig. 5 (b–d). The ZKX600 and ZKQX6000 alloys show relatively lower pole figure intensity compared to ZK60 alloy indicating weakening of the basal texture due to the additions of Ca and/or Ag.

Fig. 6 shows the image quality EBSD maps superimposed with grain orientation spread (GOS) maps of T4-treated Z6 (Fig. 6(a)) and ZK60 alloys (Fig. 6(b)). The GOS parameter, defined as the average misorientation between all pixels within a grain, helps to distinguish the deformed regions and recrystallized regions present in the microstructure [14]. A high value of misorientation spread in the microstructure implies a high geometrically necessary dislocation (GND) content corresponding to deformed regions whereas the recrystallized regions are characterized by low dislocation content having lower values of orientation spread. In this work, we have used a GOS value of $3.0°$ to separate the recrystallized and unrecrystallized grains in the ZK60 alloy. This is because the Z6 alloy has equiaxed recrystallized grains with a GOS value of less than $3.0°$ (Fig. 6(a)). Alvi et al. has shown that a GOS value of $3.0°$ is successful in distinguishing the recrystallized and unrecrystallized deformed grains [14]. In Fig. 6(b), the grains having a GOS value larger than 3.0 are shown in color (color coded as per GOS intensity levels). Based on the GOS analysis, it is seen that the ZK60 alloy has unrecrystallized grain regions up to 10% in areal fraction. Fig. 6(c) shows one of the representative unrecrystallized grains in ZK60 alloy (marked by red color rectangle in Fig. 6(b)). Upon misorientation angle analysis along the lines marked by red and violet color in Figs. 6(c), a $\sim 56°$ compression twin (Fig. 6(d)) and a $\sim 38°$ double twin (Fig. 6(e)) are present in a region marked by a red color and a violet color circles, respectively in Fig. 6(c). The EBSD (0001) pole figures of the recrystallized grains and unrecrystallized grains of ZK60 alloy are shown in Fig. 6(f) and (g), respectively. The recrystallized grains show a slight tilting of basal poles with maximum intensity along the RD whereas the unrecrystallized grains have a splitting in the poles along the RD which could be due to the presence of double twins. In a report by Kim et al. it has been shown that the splitting of basal poles towards the RD tends to be induced when deformation bands consists of double twins [15].

Fig. 7(a–d) shows the bright field TEM images of Z6, ZK60, ZKX600 and ZKQX6000 alloys after T4 treatment. ZK60 alloy shows a dispersion of fine spherical precipitates of 25.0 ± 15.0 nm in size within the grains (Fig. 7(b)). However, the Z6 alloy does not show any fine spherical precipitates (Fig. 7(a)). Interestingly, the addition of Ca as well as combined additions of Ag and Ca to the ZK60 alloy further refines the size of the spherical precipitates to 12.0 ± 5.0 nm leading to an increase in the number density of precipitates (Fig. 7(c) and (d)). The number densities of precipitates in ZK60, ZKX600 and ZKQX 6000 alloys are $2.6 \times 10^{20}\,m^{-3}$, $9.3 \times 10^{20}\,m^{-3}$ and $9.7 \times 10^{20}\,m^{-3}$ respectively. Note that the number density calculations were done as described by Underwood and the thickness of TEM foil were
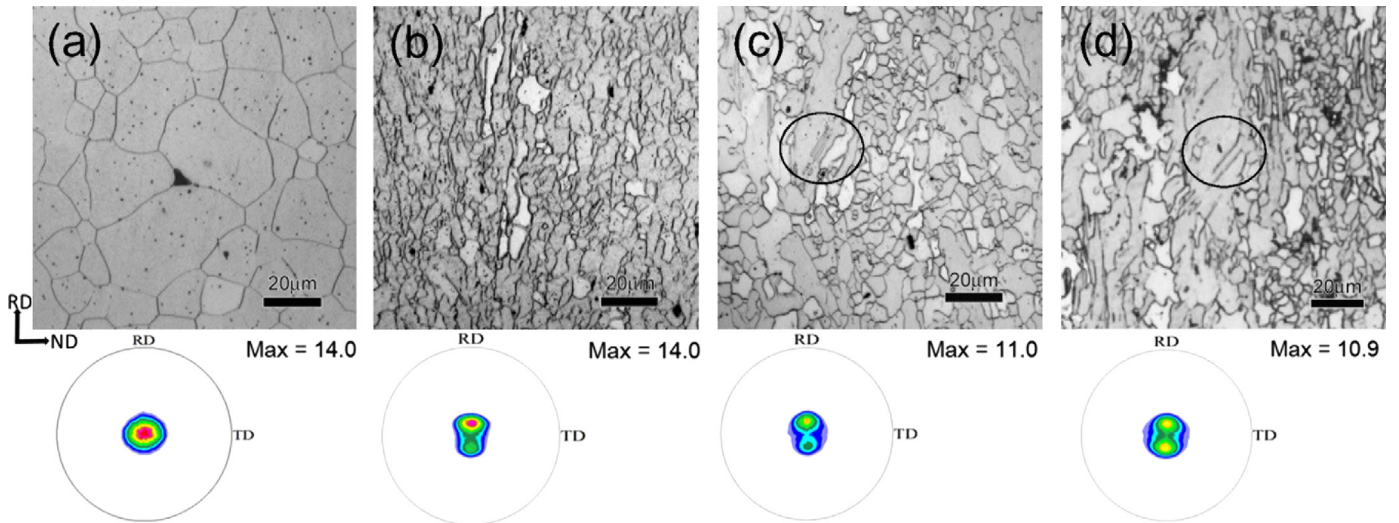
Fig. 5. Optical microstructures with corresponding (0001) pole figures from the X-ray measurements of T4 condition (a) Z6, (b) ZK60, (c) ZKX600, (d) ZKQX6000 alloys.
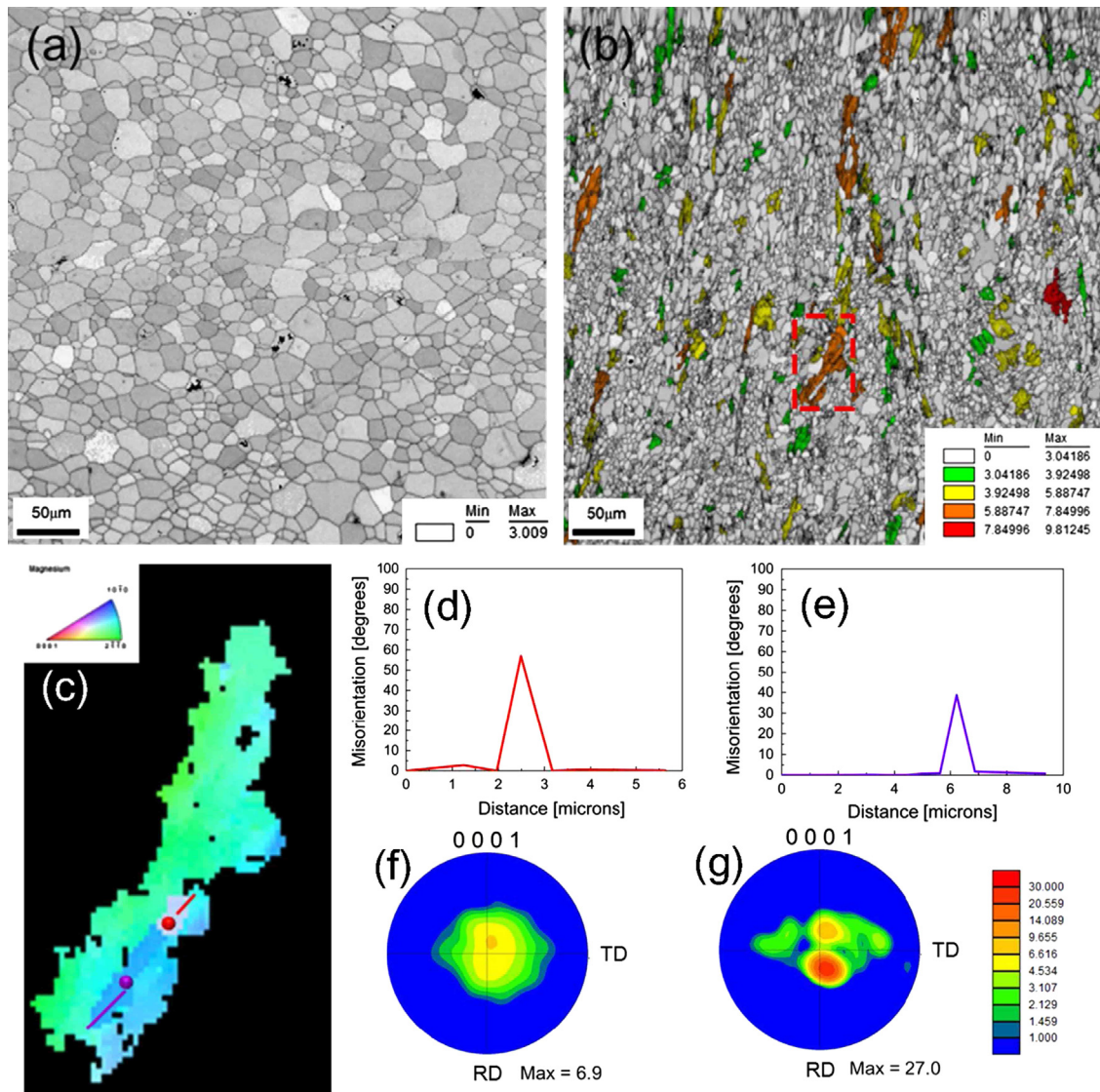

Fig. 6. Image quality EBSD maps superimposed with grain orientation spread (GOS) map of T4 condition (a) Z6 and (b) ZK60 alloy, (c) IPF map of one of the representative unrecrystallized grain (marked by a red rectangle in (b)); (d) line profile of misorientation along the red line in (c) representing compression twin; (e) line profile of misorientation along the violet line in (c) representing double twin; (f,g) (0001) EBSD pole figure of recrystallized grains and unrecrystallized grains of the T4 condition ZK60 alloy respectively. (For interpretation of the references to color in this figure legend, the reader is referred to the web version of this article.)
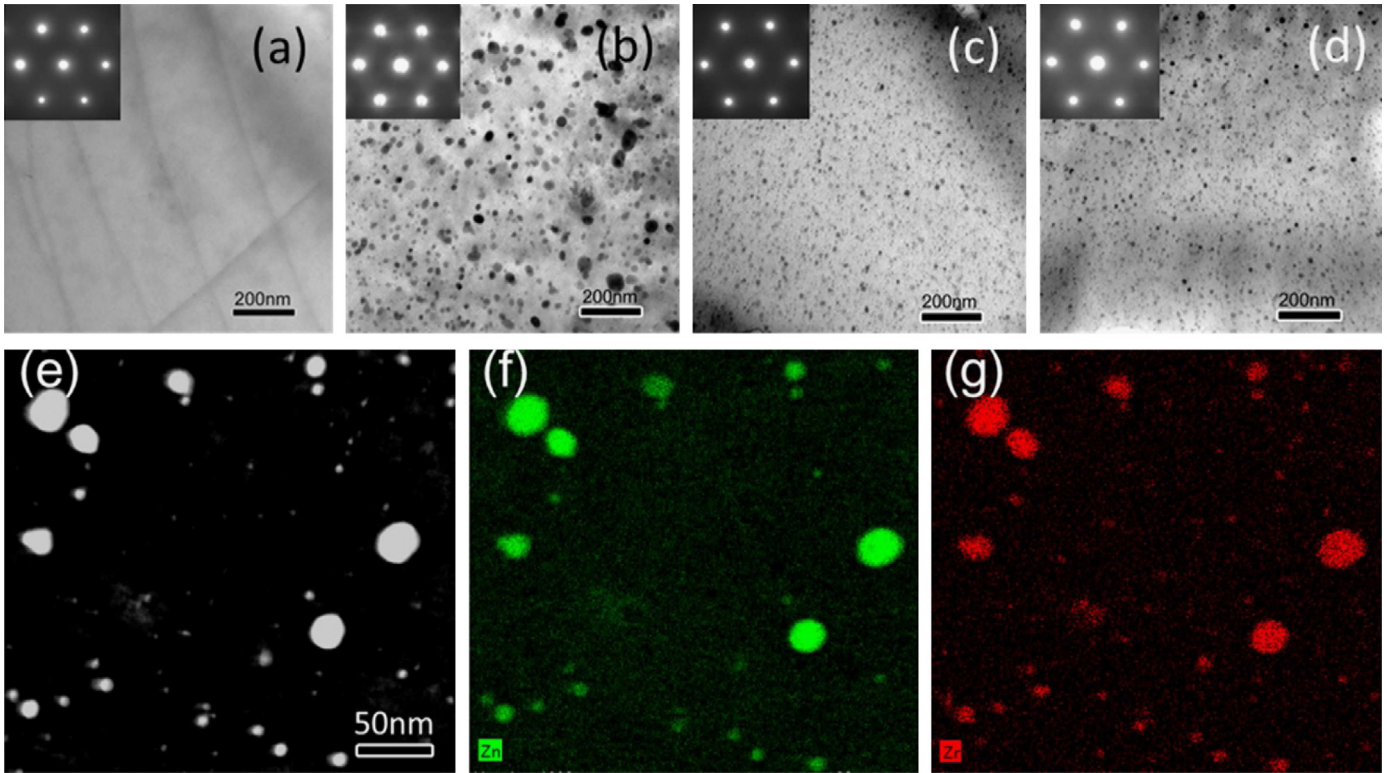
Fig. 7. Bright field TEM images of T4 condition (400 °C for 30 min) (a) Z6, (b) ZK60, (c) ZKX600, (d) ZKQX6000 alloy from the [0001] direction; (e) HAADF-STEM image of T4 condition ZK60 alloy and corresponding EDS map of (f) Zn and (g) Zr.
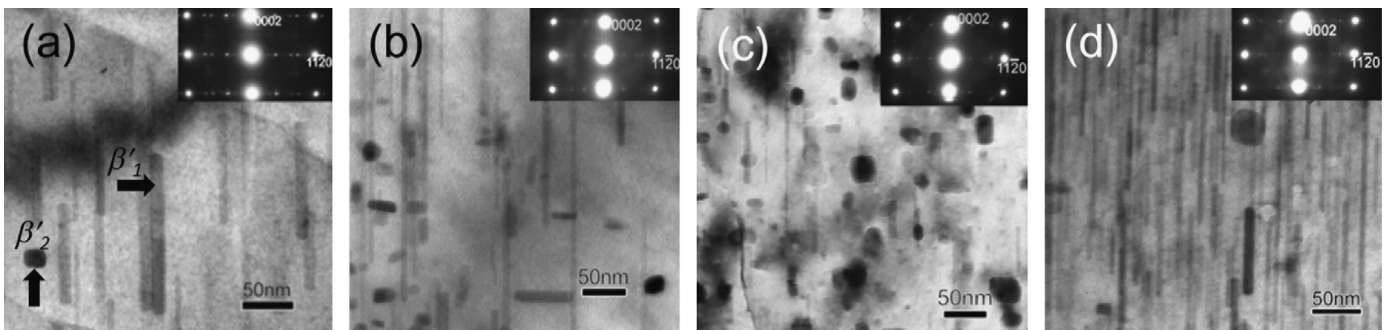

Fig. 8. Bright field TEM images of peak-aged (a) Z6 (b) ZK60 (c) ZKX600 (d) ZKQX6000 alloy from the $\langle 10\bar{1}0 \rangle$ direction.

determined by convergent beam electron diffraction analysis described by Williams and Carter [16,17]. The number density calculations show that there is a clear increase in the number density of precipitates on addition of Ca and/or Ag to ZK60 alloy whereas between ZKX600 and ZKQX6000 alloys there is only a slight difference in the number density of precipitates. Fig. 7(e) shows the high-angle annular dark-field scanning transmission electron microscopy (HAADF-STEM) image of T4 treated ZK60 alloy. The corresponding energy dispersive X-ray Spectroscopy (EDS) maps of Zn and Zr are shown in Fig. 7(f) and (g), respectively. The fine precipitates are enriched with Zn and Zr. The absence of these precipitates in Z6 alloy (Fig. 7(a)) shows that addition of Zr promotes the formation of these fine Mg(Zn,Zr) precipitates in Zr containing alloys such as ZK60, ZKX600, and ZKQX6000.

After peak aging (24 h) at 160 °C, rod-like β_1' precipitates and plate-like β_2' precipitate are observed in all the alloys (Fig. 8(a–d)). The rod-like β_1' precipitates grow along the [0001] direction (c-axis) of the matrix and the plate-like β_2' precipitates lie on the (0001) plane of the matrix. The selected area electron diffraction (SAED) patterns indicate that the β_1' precipitates have an orientation relationship of (0001) $\beta_1'//(11\bar{2}0)_{Mg}$ and $[11\bar{2}0]\beta_1'//[0001]_{Mg}$ and the

plate-like β_2' precipitates have an orientation relationship of (0001) $\beta_2'//(0001)_{Mg}$ and $[11\bar{2}0]\beta_2'//[10\bar{1}0]_{Mg}$ as previously reported [9,18].

Fig. 9(a) shows the 3DAP map of peak-aged ZK60 alloy. It reveals that there is Zr-rich region at one of the ends of the β_1' precipitates. The composition profiles of the Zr-rich and Zn-rich region of the precipitate marked by blue and black rectangles in Fig. 9(a) are shown in Fig. 9(b) and (c), respectively. The composition of the Zr-rich region is approximately Mg(Zn,Zr) and that of the Zn-rich region is ~MgZn. This indicates that the β_1' precipitates grow along the [0001] direction from the Mg(Zn,Zr) precipitates present in the T4 condition. In our previous study of a peak-aged cast ZK60 alloy, we found similar results of Zr partitioning at one of the ends of the β_1' precipitates [10].

4. Discussion

In this study, a comparative study of tensile properties and formability of TRC-HR Z6, ZK60, ZKX600 and ZKQX6000 alloys has been done by relating them with their respective microstructures and texture to understand the role of the microalloying elements.
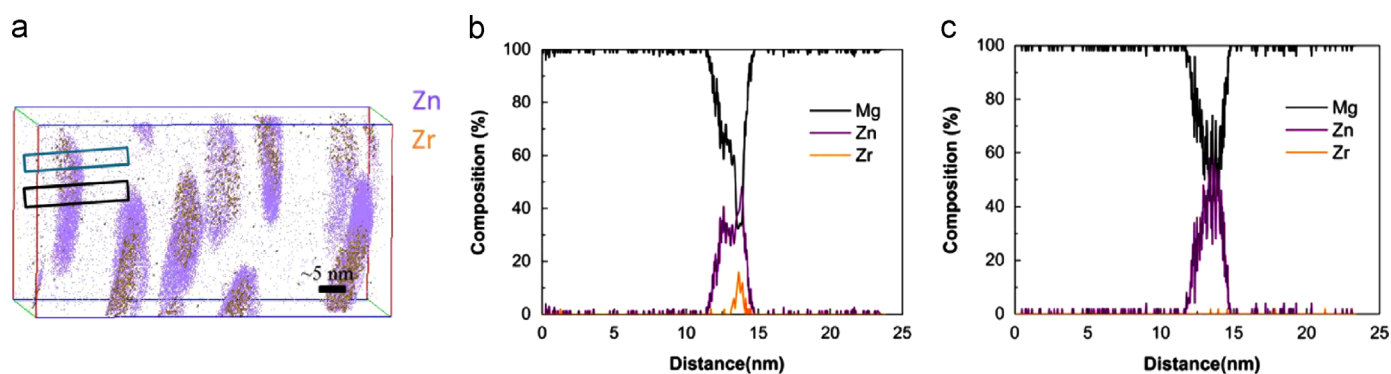
Fig. 9. 3DAP map of peak-aged (a) ZK60 alloy; (b,c) the composition profile of the Zr- and Zn-rich regions of a selected β'_1-type precipitate indicated in (a) by a blue and black rectangle respectively. (For interpretation of the references to color in this figure legend, the reader is referred to the web version of this article.)

4.1. Tensile properties and microstructure

As seen in Table 2, the addition of Zr to Z6 alloy causes an increment of more than 50 MPa in the tensile yield strength in the T4 condition. This can be attributed to the refinement of grain structure and the dispersion of the spherical Mg(Zn,Zr) precipitates. Watanabe et al., in their study on the effect of pre-strain on a ZK60 alloy, reported that there is spheroidization of the precipitates on pre-straining [19]. In the present study, the spheroidization of the precipitates can also be attributed to the high amount of strain the sheets receive during the three-pass rolling to obtain the total reduction of 50%. By the addition of Ca and the combined additions of Ag and Ca to the ZK60 alloy, the Mg(Zn,Zr) precipitates are refined and their number density increases in the T4 condition (Fig. 7(c),(d)). The elongation to failure of the ZK60 alloy slightly decreases by the addition of Ca and Ag in the T4 condition probably because of the larger number of refined Mg(Zn,Zr) precipitates. The larger number of refined Mg(Zn,Zr) precipitates are more effective in retarding the recrystallization as seen from an increase in the areal fraction of the unrecrystallized regions of the ZKX600 and ZKQX6000 alloys than in the ZK60 alloy (Fig. 5(b–d)). Oh-ishi et al., in their study of an extruded Mg–6Zn–0.4Ag–0.2Ca–0.6Zr (wt%) alloy, have also reported that the fine precipitates are effective for inhibiting dislocation motion and suppress the dynamic recrystallization leading to the formation of unrecrystallized coarse regions [9]. A recent study by Kim et al. on TRC-HR Mg–1Zn–1Ca and Mg–6Zn–1Ca (wt%) alloys have reported tensile yield strengths of 154.9 MPa and 163.6 MPa respectively in their solution treated condition (T4) [20]. The present study shows tensile yield strength in the range of 210–225 MPa in the T4 condition in all the Zr containing alloys i.e., ZK60, ZKX600 and ZKQX6000. This shows that Zr is the principal element for the increment in yield strength.

Upon peak aging, among the four alloys studied in this work, the ZKQX6000 alloy shows the highest yield strength of 300 MPa followed by ZKX600 alloy which shows yield strength of ∼290 MPa. The increase in yield strength in ZKX600 and ZKQX6000 alloys is attributed to the refinement of β'_1 and β'_2 precipitates by Ca and Ag additions thus increasing the number density of precipitates [7,21]. Since the difference in the tensile yield strength between the Ag containing ZKQX6000 alloy and Ag-free ZKX600 alloy is only ∼10 MPa, the Ag-free ZKX600 alloy looks promising for industrial application.

4.2. Texture and formability

The addition of Zr to the binary Z6 alloy increases the LDH value from 3.4 to 4.2 mm. Comparison of XRD ⟨0001⟩ pole figures of T4 treated Z6 and ZK60 alloys shows that the Z6 alloy has a strong basal texture without any splitting tendency of the basal

poles, whereas in ZK60 alloy basal poles shows tendency to split along the RD (Fig. 5(a), (b)). The splitting of basal poles along the RD in rolled magnesium alloys have been attributed to the formation of double twins in deformation bands and also due to operation of ⟨c+a⟩ slip [15,22]. Since double twin is observed in one of the unrecrystallized grains of ZK60 alloy (Fig. 6(e)), the splitting of basal poles along the RD in the present alloys is more likely to be as a result of double twinning. By the singular addition of Ca and the combined additions of Ag and Ca to the ZK60 alloy the LDH value further increases to 5.2 mm and 4.9 mm, respectively, from 4.2 mm. Thus the addition of Ca alone is sufficient for increasing the formability of the ZK60 alloy even without Ag. In a recent first-principles study by Yuasa et al., it was reported that plastic anisotropy tends to be reduced in Mg–Zn–Ca alloys due to the non-linear nature of the unstable stacking fault energy for the basal slip which gives rise to higher formability [23]. Experimental reports have also shown that the addition of Ca is beneficial for weakening texture and improvement in formability of binary Mg–Zn alloys [11,20,24]. The present work confirms that this is also the case for the ternary Mg–Zn–Zr alloys. Thus from the above results we can conclude that Ca is playing an important role in increasing the formability and that the addition of expensive Ag is not essential.

5. Conclusion

Twin roll cast and hot rolled Z6 alloys containing Zr, Ca, and Ag as microalloying elements shows tensile yield strength exceeding 300 MPa in the T6 (peak-aged) condition with reasonable formability in the T4 condition. The addition of Zr to the Z6 alloy stabilizes the fine Mg(Zn,Zr) particles which play a critical role in the recrystallization behavior. The addition of Ca to the ZK60 alloy is sufficient for weakening the basal texture and increasing the formability even without the addition of expensive Ag. Thus, the low-cost Ag-free ZKX600 alloy will be industrially promising as it shows equivalent mechanical properties to that of Ag-containing ZKQX6000 alloy.

References

[1] J. Bohlen, M.R. Nürnberg, J.W. Senn, D. Letzig, S.R. Agnew, Acta Mater. 55 (2007) 2101–2112.

[2] L. Sturkey, J.B. Clark, J. Inst. Met. 88 (1959-1960) 177–181.

[3] J.B. Clark, Acta Metall. 13 (1965) 1281–1289.

[4] E.O. Hall, J. Inst. Met. 96 (1968) 21–27.

[5] G. Mima, Y. Tanaka, Trans. Jpn. Inst. Met. 12 (1971) 71–75.

[6] C.L. Mendis, K. Oh-ishi, K. Hono, Scr. Mater. 57 (2007) 485–488.

[7] C.L. Mendis, K. Oh-ishi, Y. Kawamura, T. Honma, S. Kamado, K. Hono, Acta Mater. 57 (2009) 749–760.

[8] C.L. Mendis, J.H. Bae, N.J. Kim, K. Hono, Scr. Mater. 64 (2011) 335–338.

[9] K. Oh-ishi, C.L. Mendis, T. Honma, S. Kamado, T. Ohkubo, K. Hono, Acta Mater. 57 (2009) 5593–5604.

[10] T. Bhattacharjee, C.L. Mendis, T.T. Sasaki, T. Ohkubo, K. Hono, Scr. Mater. 67 (2012) 967–970.

[11] J.Y. Lee, Y.S. Yun, B.C. Suh, N.J. Kim, W.T. Kim, D.H. Kim, J. Alloys Compd. 589 (2014) 240–246.

[12] K. Hono, T. Ohkubo, Y.M. Chen, M. Kodzuka, K. Oh-ishi, H. Sepehri-Amin, F. Li, T. Kinno, S. Tomiya, Y. Kanitani, Ultramicroscopy 111 (2011) 576–583.

[13] D.H. Kang, D.W. Kim, S. Kim, G.T. Bae, K.H. Kim, N.J. Kim, Scr. Mater. 61 (2009) 768–771.

[14] M.H. Alvi, S. Cheong, H. Weiland, A.D. Rollett, Mater. Sci. Forum 467–470 (2004) 357–362.

[15] K.H. Kim, B.C. Suh, J.H. Bae, M.S. Shim, S. Kim, N.J. Kim, Scr. Mater. 63 (2010) 716–720.

[16] E.E. Underwood, Quantitative Stereology, Addison Wesley, Reading, MA, 1970.

[17] D.B. Williams, C.B. Carter, Transmission Electron Microscopy, 2nd ed., Springer, New York, 2009.

[18] J. Gallot, R. Graf, Comptes Rendus Acad. Sci. 261 (1965) 728–731.

[19] H. Watanabe, K. Moriwaki, T. Mukai, T. Ohsuna, K. Hiraga, K. Higashi, Mater. Trans. 44 (2003) 775–781.

[20] D.W. Kim, B.C. Suh, M.S. Shim, J.H. Bae, D.H. Kim, N.J. Kim, Metall. Mater. Trans. A 44 (2013) 2950–2961.

[21] T. Bhattacharjee, C.L. Mendis, K. Oh-ishi, T. Ohkubo, K. Hono, Mater. Sci. Eng. A 575 (2013) 231–240.

[22] R. Cottam, J. Robson, G. Lorimer, B. Davis, Mater. Sci. Eng. A 485 (2008) 375–382.

[23] M. Yuasa, M. Hayashi, M. Mabuchi, Y. Chino, Acta Mater. 65 (2014) 207–214.

[24] Y. Chino, T. Ueda, Y. Otomatsu, K. Sassa, X. Huang, K. Suzuki, M. Mabuchi, Mater. Trans. 52 (2011) 1477–1482.